Towards the best strength, ductility, and toughness combination: high entropy alloys are excellent, stainless steels are exceptional

Antoine Hilhorst* Pascal J. Jacques* Thomas Pardoen*

* UCLouvain, Institute of Mechanics, Materials and Civil Engineering (IMMC), IMAP, Place Sainte Barbe 2, Louvain-la-Neuve, 1348, Belgium

August 8, 2023

Abstract

Remarkable mechanical properties have been reported for CoCrFeMnNi-based high entropy alloys (HEAs) in recent literature, making these HEAs potentially attractive candidates for future cryogenic applications. However, the damage and fracture behaviour of HEAs is not fully understood yet, especially at low temperature. Here, the mechanical behaviour and fracture resistance of CoCrFeMnNi and CoCrNi sheets are investigated at room and cryogenic temperatures and compared to more conventional alloys. Very good properties were confirmed for HEAs, but outperformed by stainless steels under similar conditions, in terms of ductility, strength, and fracture toughness combination. Exceptional low temperature fracture energy up to 2500 kJ/m^2 was found for stainless steels compared to 700 kJ/m^2 for HEAs. A predictive model was developed and validated experimentally in order to connect the thin sheet fracture toughness to the strain hardening capacity through separating the necking and damage work spent in the fracture process zone, providing guidelines for further optimization.

1 Introduction

Humanity is facing major environmental challenges, including the need to drastically reduce the consumption of CO_2-emitting fossil fuels. Hydrogen is recognized by the International Energy Agency as a key contributor to the transition, particularly when used as reducing agent for several major industrial processes. This will result in significant increase of transport and storage of hydrogen in the years to come. However, hydrogen transport and storage technologies involve challenges to ensure safety and absence of leaking as related to the high pressures and very low temperatures [1, 2]. On shorter term, liquefied natural gas (LNG) is another option that relies on similar cryogenic technologies [3] and associated challenges. This has led to a new driving force to develop materials with optimized combination of mechanical properties, namely ductility, strength, and fracture toughness from room temperature down to at least liquid nitrogen temperature (77 K) and even down to liquid hydrogen temperature (20 K).

Most mechanical properties are temperature dependent because dislocation motion, controlling the plastic behaviour of most metals, is a thermally activated process [4]. This results in an increase of the yield strength with decreasing temperature. The effect of temperature on the strain hardening capacity and on the ductility can be either positive or negative. In the case of dislocation forest hardening, dislocation storage is relatively insensitive to temperature while dislocation recovery is temperature dependent [4]. Moreover, other dominant deformation mechanisms can be activated as a function of temperature. For example, the stacking fault energy (SFE) decreases with decreasing temperature in face centred cubic (FCC) alloys, with twinning induced plasticity (TWIP) or transformation induced plasticity (TRIP) observed over different temperature ranges [5, 6], as shown in high manganese steels [7] for instance.

Temperature also affects the fracture resistance, as quantified by the fracture toughness in mode I, J_{Ic}. Brittle failure competes with ductile failure [8, 9]. A transition from ductile to brittle behaviour occurs in some alloys as a result of the increase of the overall stress level at lower temperature (due to higher strength). The fracture toughness in the ductile regime depends on the initial level of porosity f_0, on a characteristic microstructural length X_0, as well as on the flow properties, mainly the initial yield

stress σ_0 and the strain hardening exponent n [10–12]. While temperature directly affects the mechanical behaviour, f_0 and X_0 could also be affected if a change in deformation mechanism occurs providing new void nucleation sites (e.g. twin boundaries in the case of TWIP effect, and second phase precipitation in the case of TRIP effect).

CoCrFeMnNi-based high and medium entropy alloys (HEAs and MEAs, respectively), often referred to as Cantor-based alloys, are often heralded as the next generation of alloys for cryogenic applications owing to exceptional properties and a one-of-a-kind behaviour down to liquid nitrogen temperature [13–16]. The low temperature behaviour of Cantor-based alloys has been of particular interest with the ductility, strength, as well as the fracture toughness all increasing with decreasing temperature [16, 17]. Most of these studies focused on the strain hardening behaviour, while the damage and fracture response of MEAs and HEAs are seldom reported, especially at low temperatures. Moreover, available studies essentially report fracture toughness under plane strain conditions [13, 14, 18], i.e. valid for thick sheets, while not addressing the behaviour in the near-plane stress regime, which is important for several applications. Indeed, the fracture toughness is not an intrinsic material property but depends on thickness in the case of thin sheets [19, 20]. Finally, it is important to recognize that for such high toughness alloys, the near-plane stress regime may extend to thickness well above 5 mm beyond what is commonly considered as a thin sheet.

Understanding the mechanical and damage behaviour in a thin sheet configuration is paramount to guide the development of new alloys and to assess the potential of Cantor-based medium/high entropy alloys for future cryogenic applications. Thin sheets are also important for a variety of structural applications, such as construction, storage tanks, aeroplane fuselage, and car bodies. The essential work of fracture (EWF) method is appropriate for characterizing the resistance to ductile tearing in thin sheets [21], while the fracture-mechanics-based J-integral method is essentially well defined and standardized for "thick plates" undergoing plane strain conditions [22]. Nevertheless, many studies have shown a strong correlation between the EWF and J_{Ic} [22–24].

Six alloys were investigated in this study: two Cantor-based alloys, namely CoCrNi MEA and CoCrFeMnNi HEA, two stainless steels, the 304L and 316L alloys, and two Fe-Ni alloys, an Invar alloy (Fe-36Ni) and a Fe-9Ni alloy. The four conventional alloys are all currently used in cryogenic applications. The cracking resistance is determined using the EWF method. Several ingots of CoCrNi and CoCrFeMnNi have been produced while varying the inclusion content in order to address the effect of both initial porosity f_0 and characteristic damage length X_0 on the cracking resistance. While the study of flow properties of materials at cryogenic temperature is regaining interest today, alloy design for structural applications in cryogenic environments has also been extensively promoted during the beginning of the nuclear fusion research era, from the 1960s to the 1980s [25–58]. Efforts have been made to systematically compare our new results with literature data in order to deliver a wider picture of the fracture performances of HEAs, and cryogenic alloys in general.

A good understanding of the root causes of the cracking resistance in thin ductile sheets requires partitioning the two contributions associated to damage growth and crack tip necking [20]. In order to separate both contributions, the EWF methodology is to be repeated for several thicknesses [22]. This requires a large quantity of specimens. Moreover, the sheets with different thicknesses must have identical microstructure, which is not guaranteed if they come from different thermomechanical schemes. The EWF is usually reported for one thickness per material, which does not allow distinguishing the two contributions to the work spent in the fracture process zone (FPZ). These constraints are solved in this work by proposing an experimentally validated mechanical model which quantitatively predicts the magnitude of the damage and necking work.

While Cantor-based alloys show very good properties, stainless steels outperform them at room and cryogenic temperatures, in terms of ductility, strength, and fracture toughness. This is explained on the one hand by differences in strain hardening capacity, one of the major parameter controlling both damage and necking; and on the other hand by differences in inclusion content, largely controlling the damage to cracking micromechanisms.

2 Methods

2.1 Thermo-mechanical processing

The conventional reference alloys (304L, 316L, and Invar) were processed industrially and provided as 1.5-mm recrystallized sheets. Four 1-kg ingots of CoCrFeMnNi and three 1-kg ingots of CoCrNi were processed by vacuum induction melting from pure elements. The processing conditions and raw materials varied slightly between each cast, resulting in small differences between each ingot, especially for the inclusion chemistries and volume fractions. All ingots were hot-rolled at 1273 K down to a thickness of 5 mm and subsequently cold-rolled to 1-mm or 1.5-mm thick sheets. After annealing at 1073 K for 2 hours, the microstructure was fully recrystallized. Moreover, three 2.5-kg ingots (one CoCrFeMnNi alloy, one CoCrNi alloy, and one 316L alloy) were cast with high purity elements in a dedicated re-melting induction furnace. The HEAs were subsequently processed in the same way as described above. The 316L ingot was hot-rolled at 1473 K down to 5-mm, followed by cold rolling down to a thickness of 1.5 mm. The sheets were then annealed at 1273 K for 10 minutes. The chemical composition of the principal alloying elements measured by inductively coupled plasma (ICP) is given in Table 1. The microstructures are shown in Figure 1. The detailed chemical composition of each material as well as additional SEM micrographs are provided in the Supplementary Materials.

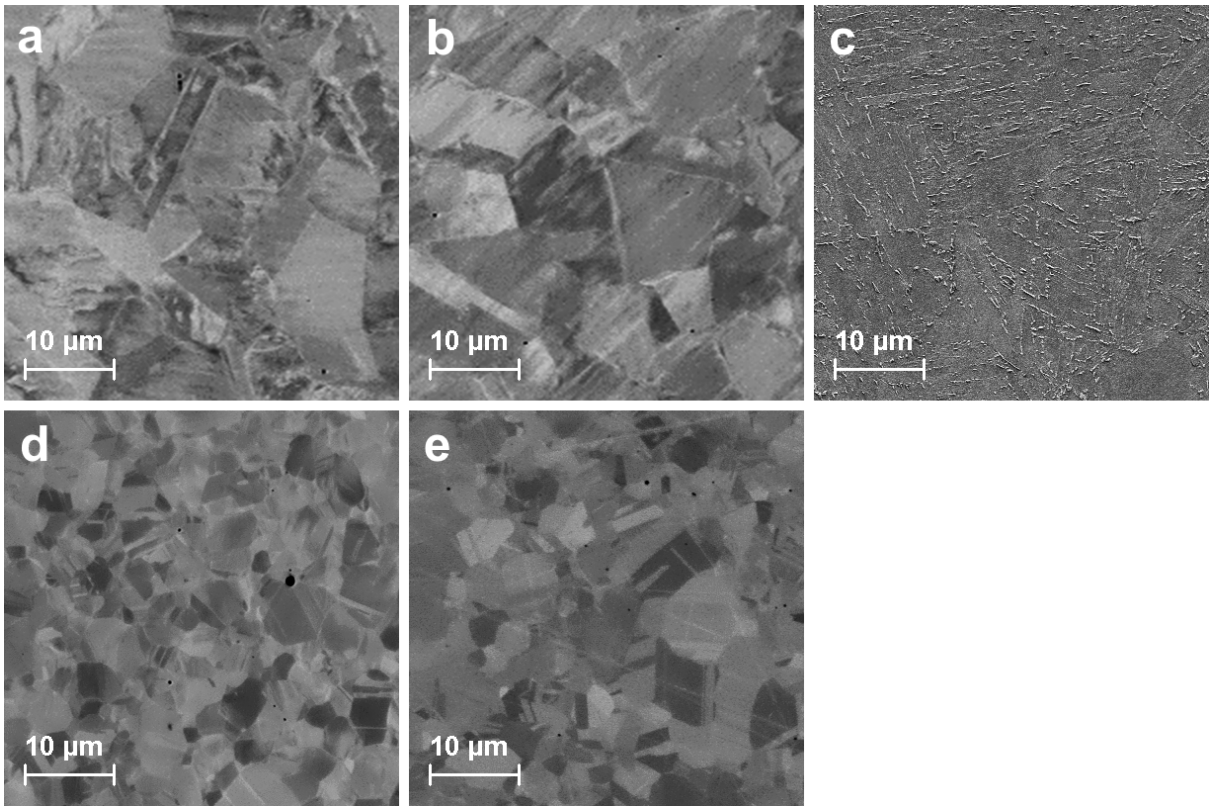

Figure 1: *Representative SEM micrographs of the microstructure of (a) 304L, (b) 316L, (c) Fe-9Ni, (d) CoCrFeMnNi, and (e) CrCoNi.*

2.2 Characterization and test methods

Microstructural characterization was based both on optical microscopy and scanning electron microscopy (SEM). The typical operating SEM parameters were 15 kV for the accelerating voltage, 60 μm aperture diameter, working distance of 6 mm, and secondary or back-scattered electrons contrast. Sample preparation followed standard practices starting with mechanical polishing with SiC papers, followed by 6 and 1 μm diamond paste polishing. The final step consisted in polishing with a solution containing silica oxide particles in suspension (OPS). The inclusion volume fraction was determined by image analysis using the software ImageJ based on light microscopy of unetched samples to improve the contrast between the metallic matrix and the non-metallic inclusions. The chemical composition of these inclusions

Table 1: *Chemical composition of the investigated alloys measured by ICP in at.%. C and S as well as N_2 and O_2 are measured separately, see the Supplementary Materials. CoCrFeMnNi and CoCrNi are referred to as HEA and MEA, respectively.*

[at.%]	304L	316L 1	316L 2	Invar	Fe9Ni	HEA 1	HEA 2	HEA 3	HEA 4	HEA 5	MEA 1	MEA 2	MEA 3	MEA 4
Co	0.19	0.24		0.04		19.9	19.2	19.0	20.2	19.6	33.2	33.2	33.1	32.8
Cr	19.0	17.8	17.7	0.07	0.03	19.9	20.5	19.6	19.5	20.3	34.0	32.8	33.2	34.2
Cu	0.30	0.25		0.05	0.02									
Fe	70.5	68.9	69.8	63.7	90.5	20.1	20.2	20.8	21.5	20.0	0.22	0.24	0.03	0.01
Mn	1.36	1.3	1.3	0.30	0.56	20.1	20.3	20.3	18.2	20.0	0.09			0.01
Mo	0.14	1.2	0.9	0.03	0.02									
Ni	7.58	9.5	9.4	34.8	8.31	20.0	19.6	19.7	20.3	19.9	33.7	33.8	33.6	33.0
Si	0.77	0.87	0.8	0.39	0.48	0.02	0.12	0.50	0.30		0.06	0.06	0.04	0.02
V	0.10													
Zn				0.17										

was measured by energy dispersive X-ray (EDX) spectrometry. The nearest neighbour distance between inclusions was determined by Delaunay triangulation (the dual of the Voronoi diagram) of the inclusion positions in several images. The inclusion characterization for each investigated alloy is given in the Supplementary Materials.

Flat dog-bone tensile samples with a total length of 70 mm, total width of 20 mm, a 30 mm gauge length and 6 mm gauge width were machined by electrical discharge machining and deformed at a cross-head speed of 1 mm/min, equivalent to a strain rate of $\sim 6\ 10^{-4} s^{-1}$ ensuring isothermal testing conditions. The engineering and true stress-strain curves were calculated from the force-displacement measurements. The true fracture stress σ_f is estimated by recording the force at fracture F_f, determined by the sudden sharp and unstable drop of the force, as well as by measuring the cross-section area at fracture A_f, following the relationship $\sigma_f = F_f/A_f$. The true fracture strain is determined as $\epsilon_f = \ln(A_0/A_f)$, with A_0 the initial cross-section area. The cross section area used to compute the true fracture strain was measured as the projected fracture surface imaged by SEM. The uncertainty on both ϵ_f and σ_f is about 15% for flat specimens [59–61]. To characterize the dimple size and spacing, SEM micrographs of the fracture surface were processed by adjusting the contrast and brightness of the image, applying a threshold to highlight the dimple edges, then using a succession of binary operations to extract the boundaries. Once this image transformation was performed, the position and size of each dimple can be extracted. Similarly to the inclusion analysis, a Delaunay triangulation was used to compute the average nearest neighbour distance between dimples, known to be a good indicator of the internal length X_0 [11].

2.3 Essential work of fracture method

The essential work of fracture method, introduced by Cotterell and Reddel [62] in 1977, based on the work of Broberg [63, 64], is an alternative to the determination of the J integral at cracking initiation J_{Ic} to characterize the cracking resistance. The principle is to separate the work necessary for damage and necking in the FPZ, w_e, named EWF, from the non-essential plastic work, w_p. Indeed, the plastic region surrounding the crack tip can be divided into a diffuse plastic region, which scales with the ligament length, and in an end region, called the FPZ, where necking and damage take place, which scales with thickness. As the two quantities scale differently, they can be separated using geometrically similar specimens of different sizes, see details in [21, 62, 65] and the schematic representation in Figure 2. The EWF method quantifies the work spent in the FPZ as an average over the entire crack propagation stage while J_{Ic} quantifies the value at cracking initiation. Even though some early studies showed the equivalence between J_{Ic} and w_e [22, 24], this is not rigorously true if the cracking conditions inside the FPZ significantly vary between initiation and steady crack propagation [23, 66]. The EWF method presents several advantages over standardized fracture mechanics tests. The determination of the exact initiation of cracking and the crack extension are not necessary for the EWF method; only the load-displacement curve is needed. Furthermore, the (sometimes) difficult issue of starting with a perfectly sharp pre-crack (requiring fatigue pre-cracking) is not as severe as in fracture mechanics testing. However, several specimens have to be tested in order generate the accurate linear fit from which the EWF is extracted, requiring a large quantity of material needed to estimate the EWF. An improved EWF methodology to reduce the quantity of materials while retaining the same error on the extracted EWF has been used in this work, see [67].

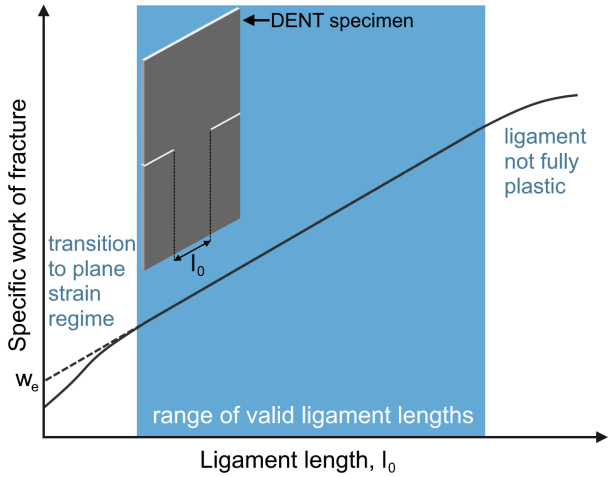

Figure 2: *Representation of the total work normalized by the initial ligament area (the specific work of fracture) as a function of the ligament length l_0 for a series of geometrically similar DENT specimens. The geometry of a DENT specimen is pictured schematically. The EWF (w_e) corresponds to the constant term of the linear regression performed over the valid ligament length range.*

3 Model to partition the fracture energy

The core principle of the EWF method is the partitioning between w_e (J/m^2), the specific work accounting for both the damage and necking energy spent in the FPZ, and w_p (J/m^3), the work of plasticity spent in the diffuse plastic zone. Now, w_e can be further divided into the work of fracture, Γ_0 (J/m^2), and the work of necking, Γ_n (J/m^2) [21–23]. The assumption is that Γ_0 is independent of the sheet thickness in the near plane stress regime and that Γ_n varies linearly with the sheet thickness as the necking zone height scales proportionally to thickness. Models have been proposed earlier to capture the key effects contributing to both the work of damage and of necking entering the EWF [20–22]. The model for Γ_n has been adapted and extended to the alloys investigated in this work in order to properly account for their very large strain hardening capacity.

The damage contribution, Γ_0, has been predicted using an extended Gurson-type approach [68] supplemented by a void coalescence criterion assuming a material made of regularly distributed spheroidal cavities with an initial spacing X_0 and initial volume fraction f_0. This version of the Gurson model thus neglects any void nucleation stage that could delay the damage evolution. Γ_0 was found (see also later) to significantly depend on n, hence $\Gamma_0 \equiv f_1(X_0, \sigma_0, f_0, n)$. By fitting the results of Pardoen et al. [20] extracted from finite element simulations of plane strain tension specimens undergoing necking (which is the stress state representative of the FPZ in a thin sheet [69]), one can express the work of damage Γ_0 as

$$\log_{10}\frac{\Gamma_0(n, f_0, \sigma_0, X_0)}{\sigma_0 X_0} = 0.54 + \frac{1.39}{\log_{10}(f_0)} - 0.1\log_{10}(f_0) + 4.02n. \quad (1)$$

The term Γ_n is modelled by assuming that the total work dissipated in the neck occurs in an active volume with a height decreasing continuously with decreasing thickness of the active necking zone, as schematically drawn in Figure 3(a). The hardening law and the ratio between height and thickness of the active necking region α must be known to estimate the magnitude of Γ_n. The expression of Γ_n is given by

$$\Gamma_n = t_0 \alpha w_n, \quad (2)$$

$$\alpha w_n = \frac{2}{h_{u0}} \int_0^{h_{u0}/2} \int_{\bar{\epsilon}_u}^{\bar{\epsilon}_n^{max}} \bar{\sigma}\, \mathrm{d}\bar{\epsilon} \mathrm{d}h. \quad (3)$$

where $\bar{\sigma}$ is the equivalent norm of the Cauchy stress tensor, $\bar{\epsilon}$ is the equivalent strain, w_n is the average work of necking per unit volume, t_0 is the initial thickness, h_{u0} is the height of the neck at the beginning of necking, $\bar{\epsilon}_u$ and $\bar{\epsilon}_f$ are the equivalent uniform strain and fracture strain, respectively, and $\bar{\epsilon}_n^{max}(h)$ is the maximum equivalent strain attained in the layer located at a distance h from the mid-plane of

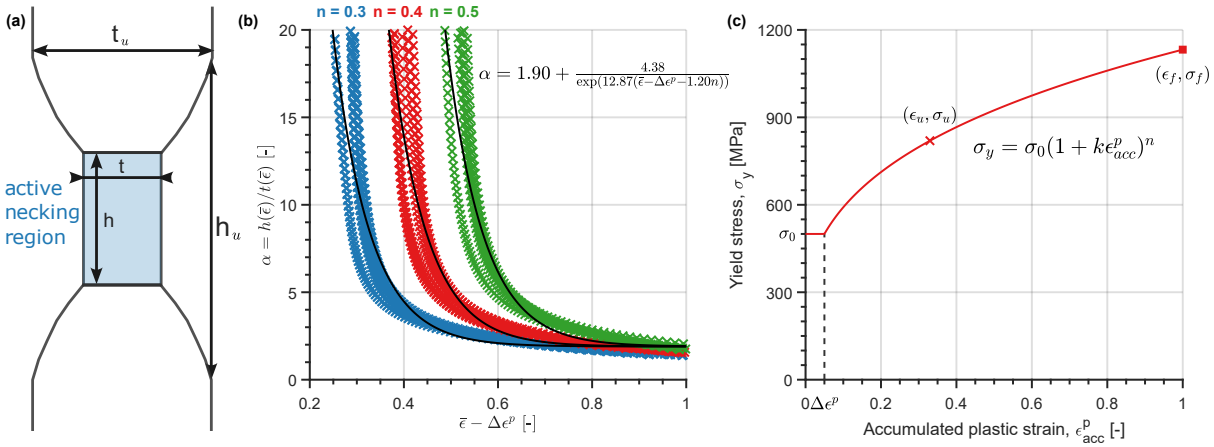

Figure 3: *Model for the work of necking. (a) Schematic representation of the active necking region with t_u, h_u, the thickness and height, respectively, at the onset of necking, and t, h, the current thickness and height of the necking region; (b) variation of the height over thickness ratio for the necking region as a function of the strain. Markers correspond to finite element simulations for a range of k, n, and $\Delta\epsilon^p$ parameters; (c) an example of the modified Swift hardening law for $\Delta\epsilon^p = 0.05$, $k = 15$ and $\sigma_0 = 500$ MPa.*

the neck. The parameter α is estimated by running finite element (FE) simulations under plane strain tension conditions with the software ABAQUS. A modified Swift hardening law is assumed, as described by

$$\sigma_y = \sigma_0 \qquad \text{for } \epsilon^p_{acc} < \Delta\epsilon^p, \tag{4}$$

$$\sigma_y = \sigma_0(1 + k(\epsilon^p_{acc} - \Delta\epsilon^p))^n \qquad \text{for } \epsilon^p_{acc} \geq \Delta\epsilon^p, \tag{5}$$

where σ_y is the current yield stress, σ_0 is the initial yield stress, ϵ^p_{acc} is the accumulated plastic strain, and k, $\Delta\epsilon^p$ and n are fitting parameters, as shown in Figure 3(c). The parameter n is the average strain hardening exponent. The parameter $\Delta\epsilon^p$ was introduced to account for the plateau observed in some alloys (see Section 4). The FE model is a sheet of thickness t and height $H >> h$ deformed under plane strain conditions relying on J_2 plasticity and isotropic elasticity. The evolution of the aspect ratio of the neck α, shown in Figure 4(b), is extracted at different levels of deformation $\bar{\epsilon}$ and this for different hardening laws characterized by different n, k, and $\Delta\epsilon^p$ values. The following empirical fit accurately captures the variation of α with the hardening parameters:

$$\alpha = \frac{h(\bar{\epsilon})}{t(\bar{\epsilon})} = 1.896 + \frac{4.378}{\exp(12.87((\bar{\epsilon} - \Delta\epsilon^p) - 1.196n))}. \tag{6}$$

The equivalent strain at a given thickness t is expressed in plane strain as

$$\bar{\epsilon} = \frac{2}{\sqrt{3}} \ln\left(\frac{t_0}{t}\right). \tag{7}$$

Additionally, volume conservation imposes that

$$t(\bar{\epsilon}_1)h(\bar{\epsilon}_1) = t(\bar{\epsilon}_2)h(\bar{\epsilon}_2). \tag{8}$$

From Equations (6-8), the maximum equivalent strain attained in the layer located at a distance h from the mid-plane of the neck, $\bar{\epsilon}^{max}_n(h)$, can be calculated as

$$\bar{\epsilon}^{max}_n(h) = \bar{\epsilon}_f \qquad \text{for } h < h_{f0}/2, \tag{9}$$

$$\bar{\epsilon}^{max}_n(h) = \frac{2}{\sqrt{3}} \ln\left(\frac{t_0\sqrt{\alpha(\bar{\epsilon}^{max}_n(h))}}{\sqrt{ht_0}}\right) \qquad \text{for } h_{f0}/2 \geq h \geq h_{u0}/2, \tag{10}$$

$$\bar{\epsilon}^{max}_n(h) = \bar{\epsilon}_u \qquad \text{for } h > h_{u0}/2, \tag{11}$$

where h_{f0} is the height of the neck at fracture. Finally, integrating Γ_n gives

$$\Gamma_n = \frac{2t_0\sigma_0}{kh_{u0}(n+1)}\left(\frac{h_{f0}}{2}(1+k(\bar{\epsilon}_f-\Delta\epsilon^p))^{n+1}-\frac{h_{u0}}{2}(1+k(\bar{\epsilon}_u-\Delta\epsilon^p))^{n+1}+\ldots \int_{h_{f0}/2}^{h_{u0}/2}(1+k(\bar{\epsilon}_n^{max}(h)-\Delta\epsilon^p))^{n+1}\,dh\right). \quad (12)$$

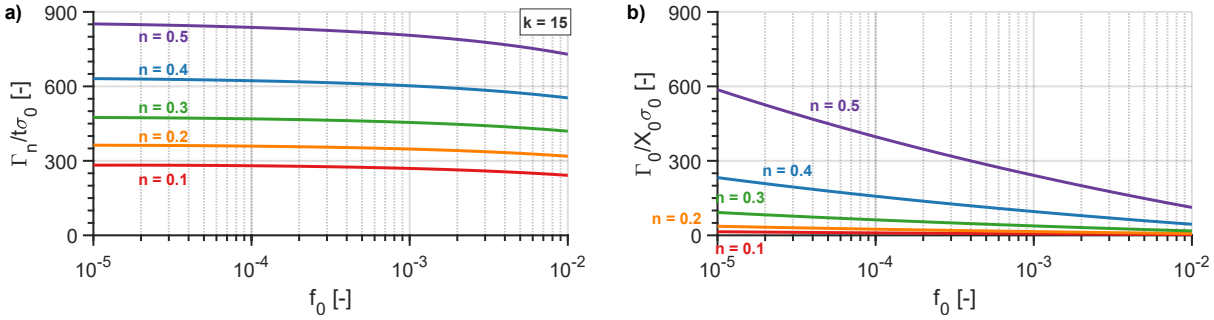

Figure 4: *Variation of (a) the work of necking, Γ_n, normalized by the sheet thickness t and the initial yield stress σ_0, for $k = 15$, and of (b) the work of damage, Γ_0, normalized by the characteristic length X_0 and the initial yield stress σ_0 as a function of the strain hardening n and the initial void volume fraction f_0, according to the proposed model.*

Figure 4 shows the variation of Γ_n normalized by $t_0\sigma_0$ and of Γ_0 normalized by $X_0\sigma_0$ as a function of the initial void volume fraction f_0. To draw the behaviour of Γ_n, the equivalent uniform strain and equivalent fracture strain, $\bar{\epsilon}_u$ and $\bar{\epsilon}_f$, respectively, as needed for Equation 12, are estimated using

$$\bar{\epsilon}_u = \frac{2nk-\sqrt{3}(1-k\Delta\epsilon^p)}{\sqrt{3}k}, \quad (13)$$

$$\bar{\epsilon}_f = -0.66+3.49n-0.58\log_{10}(f_0)-4.04n^2-0.06\log_{10}(f_0)^2-0.39n\log_{10}(f_0), \quad (14)$$

with Equation 14 directly fitted on the results of [20], as obtained using an extended Gurson model. The proof of equation 13 is detailed in the Supplementary Materials. Figure 4(a) shows that the work of necking Γ_n is sensitive to the degree of work hardening n and k, as well as on the initial void volume fraction f_0 (coming indirectly in Equation 12 through the fracture strain $\bar{\epsilon}_f$). Γ_0 is proportional to $X_0\sigma_0$ and depends on n and f_0, but is independent on k. Figure 4 is provided to illustrate the effect of the different parameters and to reveal the key role of n on setting the magnitude of both Γ_0 and Γ_n. Note already that, when using this model later to analyse the experimental data, one will not use $\bar{\epsilon}_u$ and $\bar{\epsilon}_f$ from Equations 13 and 14 but directly the experimental values. Indeed, the $\bar{\epsilon}_f$ of Equation 14 does not account for several effects such as delayed void nucleation that would lead to a higher $\bar{\epsilon}_f$ or such as void distribution effects that would reduce $\bar{\epsilon}_f$.

The strength of this model, once α has been calibrated, is the absence of fitting parameters with only material properties determined from a single uniaxial tensile test. The plastic behaviour (σ_0, n, and k) is obtained by fitting the true stress-true (plastic) strain response before the onset of necking with the modified Swift law; X_0 is estimated as the mean nearest neighbour distance between dimples, measured by image analysis of several (flat) areas of the fracture surface; and the initial volume fraction of porosity f_0 is assumed to be equal to the volume fraction of inclusions. The uniform strain can be obtained from the stress-strain response (to avoid the use of Equation 13) while the fracture strain is determined by measuring the final cross section area A_f on the fracture surface (to avoid the use of Equation 14), see Methods. The characteristic length X_0 is assumed independent of the test temperature, as this parameter is evaluated from the fracture surface of tests performed at room temperature. This means that the damage evolution is controlled by the same mechanisms in this range of temperature.

4 Results

4.1 Elastoplastic behaviour

Figure 5 shows the variation of the flow properties up to the onset of necking and the extrapolated stress-strain values at fracture for all investigated grades at room and cryogenic temperatures. All the alloys exhibit low to moderate yield strength. The effect of the temperature on the strength levels is quite pronounced, doubling for the stainless steels and the Invar from 293 K to 77 K. The increase in strength is less pronounced for CoCrFeMnNi and CoCrNi alloys, but is still significant. Here, the ductility is expressed by two different quantities: the true uniform strain ϵ_u, a simple formability indicator for processes limited by plastic localization, represented by crosses in Figure 5; and the true fracture strain ϵ_f (which is equal to $\bar{\epsilon}_f$ in the case of uniaxial tension), which characterizes the capacity of the material to deform without cracking, represented by squares in Figure 5. All alloys investigated in this study show a large ductility at room and cryogenic temperatures. The uniform strain of the stainless steels and Fe-Ni alloys is reduced when decreasing the temperature, while the CoCrFeMnNi and CoCrNi alloys show a significant increase in true uniform strain from 0.30 at 293 K to 0.44 at 77 K. All the investigated alloys also present very large deformation at fracture in the range of test temperatures: at room temperature, ϵ_f is close to 1 for both CoCrFeMnNi and CoCrNi (this represents an engineering strain of $\approx 170\%$), around 1.25 for 304L, and 316L, and reaches an extremely large value of 2.34 for the Invar alloy. At cryogenic temperature, ϵ_f remains large for all alloys. None of the six materials tested in this work shows ϵ_f larger at cryogenic temperature. CoCrFeMnNi and CoCrNi alloys present the smallest reduction of fracture strain with decreasing temperature. In order to compare the flow properties, true stress and true strain values are reported, unless stated otherwise. More details are provided in Supplementary Materials such as the engineering stress-engineering strain curves.

These alloys are then compared to many other metallic alloys that have been studied in the context of low temperature applications. Figures 6(a, c) show the yield strength and Figures 6(b, d) show the ultimate tensile strength as a function of the true uniform strain at room and liquid nitrogen temperature, respectively. These graphs illustrate the trade-off between strength and ductility with some alloys escaping from the so-called "banana" trend [9]. The literature [16, 70] insists on the increase of the ductility with decreasing temperature for Cantor-based alloys. The present results show that it is indeed the case for the uniform elongation of CoCrFeMnNi and CoCrNi. However, a similar behaviour can be found across many different families of metallic alloys, as there exists many (stainless) steels, iron-nickel alloys, superalloys (nickel-, cobalt-, or iron-based), and titanium and aluminium alloys that behave similarly, as shown in Figures 6(a-d). Figure 6(d) also reveals that Cantor-based alloys are among the best materials at 77 K alongside stainless steels.

4.2 Toughness and fracture resistance under near-plane-stress conditions

The characterization of the damage resistance is often neglected in alloy development, mostly focussing on strength and ductility. "Toughness", in the metallurgy community, often refers to the total work dissipated until failure of the material during a tensile test. The toughness corresponding to the full energy expenditure until fracture (per unit volume) is approximately given by the work of fracture $W_f = \frac{1}{2}(\sigma_0 + \sigma_u)\epsilon_u + \frac{1}{2}(\sigma_u + \sigma_f)(\epsilon_f - \epsilon_u)$ [71]. However, toughness must not be confused with fracture toughness. In this work, the fracture toughness was characterized through the EWF method, which aims at extracting the average work per unit area spent in the FPZ from initiation to propagation using dimensional considerations [20, 21]. Figure 7 compares the work of fracture W_f ("toughness") and EWF results of the investigated materials together with results from literature [20, 22, 62, 65, 67, 72–84] as a function of uniform strain. The full data from which the EWF of each alloy was extracted are given in the Supplementary Materials. To the authors' knowledge, it is the first time that EWF results are reported for cryogenic temperatures. Note that the properties ϵ_f and σ_f from which W_f can be estimated are unfortunately rarely reported in the literature, explaining the limited number of data.

Stainless steels show the largest W_f both at room and low temperatures, while Cantor-based alloys show moderate to high W_f with similar ductility. Conventional steels and iron-nickel alloys also show high W_f values spreading over a large range of ductility. At cryogenic temperature, these steels and Fe-Ni alloys still exhibit high W_f values, albeit with lower ductility than stainless steels or Cantor-based alloys. The CoCrFeMnNi and CoCrNi alloys noticeably show enhanced W_f and ductility at 77 K compared to

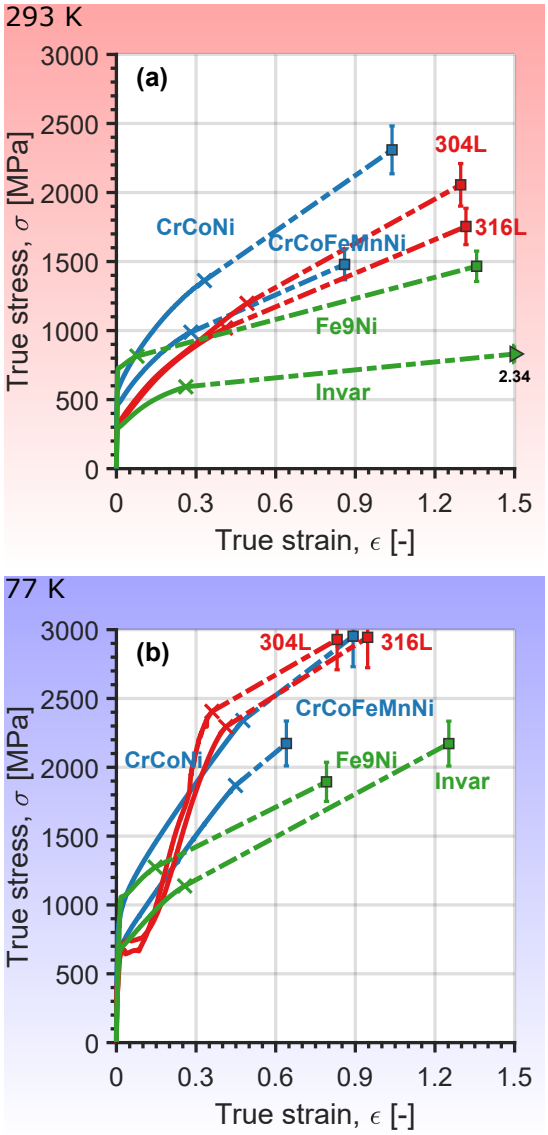

Figure 5: *Flow properties of Cantor-based alloys and conventional alloys at room and cryogenic temperatures in terms of representative tensile curve for each of the six investigated alloys: CoCrNi, CoCrFeMnNi, 304L, 316L, Fe9Ni and Invar, at (a) room and (b) cryogenic temperatures, respectively. The dotted curves relate the stress-strain values at the onset of necking to the stress-strain values at fracture, estimated from the force and the cross-section area at fracture.*

room temperature.

All materials in this study show very high cracking resistance at room temperature, with w_e above 465 kJ/m^2 for 1.5-mm-thick sheets. The EWF values measured for the CoCrFeMnNi HEA are smaller than for the ternary counterpart. At 1-mm thickness, w_e is equal to 360 kJ/m^2 for CoCrFeMnNi, and 625 kJ/m^2 for CoCrNi. For a 1.5-mm thickness, the difference is less significant, with values ranging from 465 to 575 kJ/m^2 for CoCrFeMnNi and values ranging from 555 to 705 kJ/m^2 for CoCrNi. The conventional stainless steels demonstrate exceptional fracture resistance with w_e ranging from 723 to 1060 kJ/m^2, respectively, for 1.5-mm thickness. The Invar also displays a high fracture resistance, with $w_e \approx 500$ kJ/m^2.

Although care should be taken when analysing the results at low temperature due to the small number of samples and to the variability, one can qualitatively assess the performance of these alloys. A startling observation is the EWF values for 304L and 316L, reaching ~2500 kJ/m^2. This is, to our knowledge, the largest fracture resistance ever measured for a material, at least with the EWF method fulfilling all criteria of validity. Part of the reason for this remarkable cracking resistance is the near plane stress

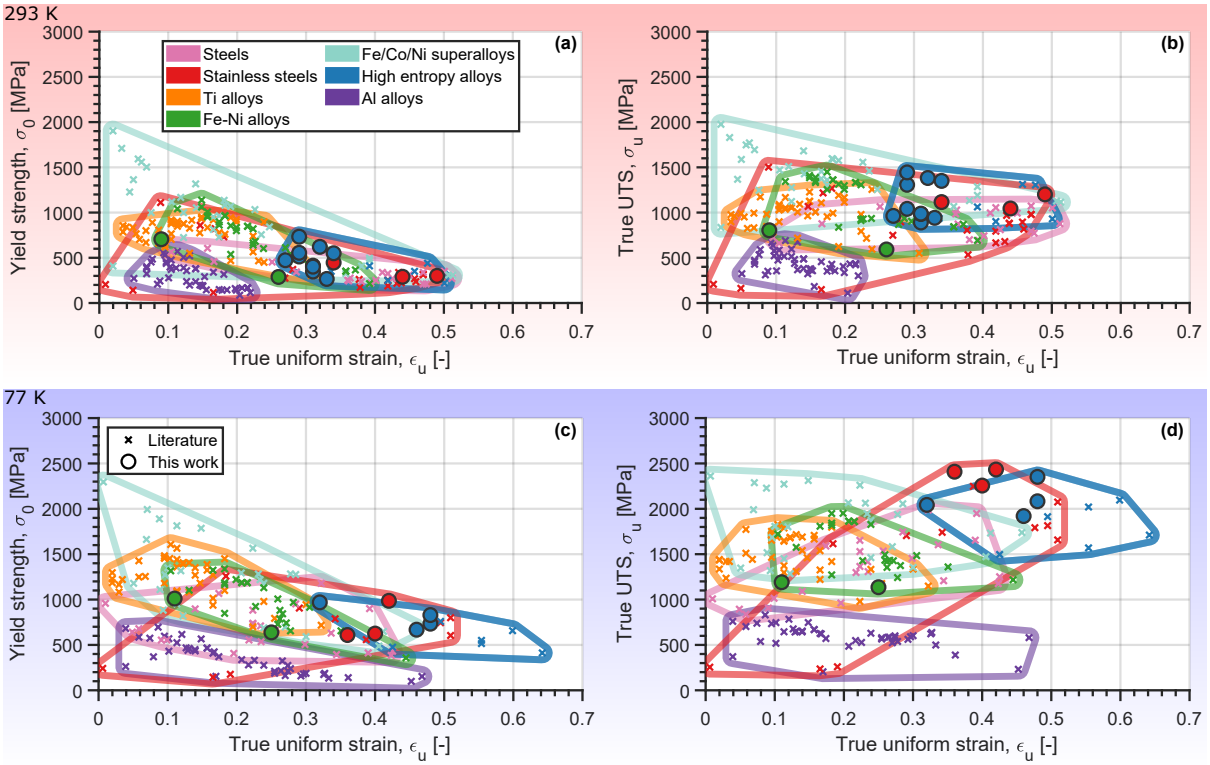

Figure 6: *Flow properties of Cantor-based alloys and conventional alloys at room and cryogenic temperatures in terms of (a, c) yield strength and (b, d) true ultimate tensile strength as a function of the true uniform strain of the investigated alloys as well as other alloys used for cryogenic applications [25–58], at (a, b) room and (c, d) cryogenic temperatures.*

conditions as further discussed next. Furthermore, all tested alloys keep very good cracking resistance at low temperature. Indeed, the alloys for which a direct comparison can be made, w_e is larger at 77 K, except for CoCrNi. Except for stainless steels, the EWF values range from ~300 to ~600 kJ/m^2 at cryogenic temperature.

4.3 Model predictions

One element of complexity when addressing the fracture resistance of thin sheets is the thickness dependence, making more complicated the direct comparison of results obtained for one material to another if not corresponding to the same thickness. Indeed, the stress state changes with the thickness in a cracked metal sheet. The stress state of thick specimens undergoes plane-strain conditions over most of the crack front (no deformation in the thickness direction), while the stress state near the crack tip of thin specimens is close to pure plane stress (but with a plane-strain state with respect to the ligament direction [85]). The ductile damage mechanism is dependent upon the stress triaxiality, which is much lower in the near-plane-stress regime, hence, the fracture toughness is geometry dependent [22, 23]. This dependence is further amplified by the work of necking Γ_n which, if present, also depends on thickness. The fracture toughness of ductile metals is almost always larger under near-plane-stress conditions compared to plane strain, with a maximum attained at an intermediate thickness [86]. By modelling both the necking and damage contributions to the EWF, the cracking resistance of thin sheets can be further analysed to unravel the root causes of the excellent performances of some alloys compared to others. Figure 8 compares the contributions of Γ_0 and Γ_n to the EWF for each of the investigated alloys. The model predicts, based on the experimental hardening law and $\bar{\epsilon}_f$, remarkably well the EWF values, within 17% of error for the worst case, and captures the relative behaviour of the investigated alloys (Fig. 8(a)). According to the model, Γ_0 depends only on the initial porosity, on a characteristic length, on the strain hardening coefficient, and on the yield strength. In terms of strength and ductility, HEAs are not better than stainless steels. It is worth emphasizing that the industrial alloys studied in this work have a particularly lean inclusion content, with very low $1/X_0$ and f_0 levels, explaining the large values of the damage work Γ_0. The work of necking, Γ_n, is primarily dependent on the strain hardening

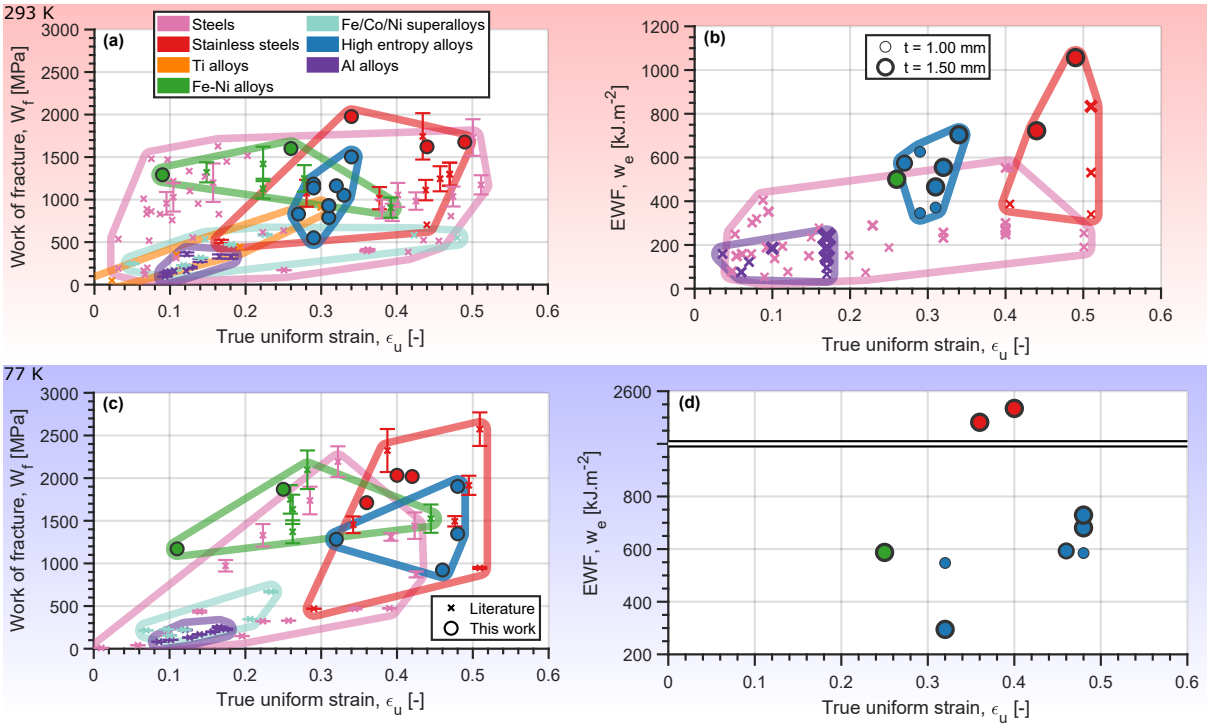

Figure 7: *Toughness, represented by the work of fracture W_f (J/m^3) per unit volume in tension, and fracture resistance, expressed by the essential work of fracture w_e (J/m^2), of Cantor alloys compared to conventional materials [25–58, 71]; (a) and (c) represent the work of fracture as a function of the true uniform strain at room and cryogenic temperatures, respectively; (b) and (d) correspond to the essential work of fracture as a function of the true uniform strain for different sheet thicknesses of the alloys investigated in this work, at room and cryogenic temperatures, respectively. Marker size indicates the sheet thickness. The room temperature values are compared with available literature data [20, 22, 62, 65, 67, 72–84].*

(through both n and k), explaining, in a relatively simple way, the differences. Particularly for 304L and 316L deformed at low temperature, the exceptionally high work of necking is attributed to the increasing work hardening capacity with decreasing temperature (see Fig. 5(b)) is responsible for a large necking region capable of dissipating a large amount of energy. This very large necking region has also been confirmed experimentally. Indeed, profilometry measurements confirm that a high n leads to a necking region that is very elongated (several times the thickness), which increases Γ_n (at least for the strains below 0.3).

Thanks to this model, the cracking resistance of fictitious alloys can also be compared assuming they had the same sheet thickness, inclusion content and initial porosity. For a 1.5-mm-thick sheets with $X_0 = 1.5$ μm, $f_0 = 0.1\%$, and no strain plateau, the model predicts an EWF of 480 and 750 kJ/m^2 for CoCrFeMnNi, 630 and 950 kJ/m^2 for CoCrNi, and 750 and 1120 kJ/m^2 for stainless steels at room and cryogenic temperatures, respectively.

5 Discussion

In Cantor-based HEAs, the excellent mechanical properties and the effect of temperature are attributed to the mechanical twinning mechanism [87]. In the present work, twinning was observed for the alloys 316L, CoCrFeMnNi, and CoCrNi at room and cryogenic temperatures, activated for lower strains at 77 K (see "Supplemetary Materials" for details). Moreover, the formation of martensite also occurs in 316L for samples deformed at 77 K for strains typically below 0.3 explaining the boost of strain hardening in this deformation regime, see Fig. 5(b). The combination of the TRIP and TWIP effects explains the excellent strength and ductility balance at low temperature, comparable or even superior to the properties of the MEAs and HEAs. A TRIP effect with the formation of a HCP phase was also found in CoCrNi at room temperature, following the Mahajan twin nucleation and growth mechanisms [88, 89].

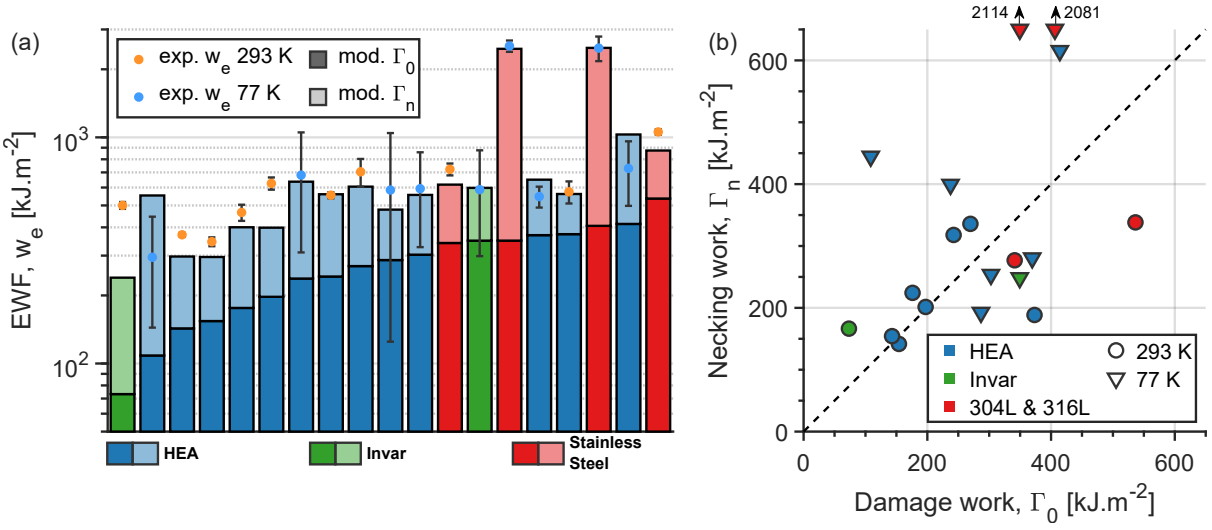

Figure 8: *(a) Comparison of the measured and modelled EWF for the alloys investigated in this work and (b) other view on the* Γ_0 *and* Γ_n *relative contribution.*

The deformation mechanisms of the Invar, Fe-9Ni and 304L were not studied in details. However, their deformation behaviour is well known, being dominated by dislocation glide at room temperature and with the additional activation of a TWIP effect in Invar [90] and a combined TWIP and TRIP effects in 304L [91] at cryogenic temperature.

The popularity of HEAs in the context of fracture resistance was partly motivated by the results of Gludovatz et al. [13, 14] reporting "exceptional" mechanical properties at low temperatures. These results were compared to conventional alloys using Ashby maps, giving a proper appraisal of commercialized materials in conventional operating conditions (*e.g.* room temperature), though not including state-of-the-art cryogenic alloys. Our present analysis shows that several reference conventional alloys can compete or even surpass MEAs and HEAs in terms of mechanical properties at room and cryogenic temperatures. The quinary CoCrFeMnNi and the ternary CoCrNi outperform the other alloys when focussing on uniform deformation. However, an increasing ductility with decreasing temperature is not an anomaly or specificity of the Cantor alloys, as this behaviour is observed in several other alloys.

Gludovatz et al. [13, 14] also reported that the fracture toughness of CoCrFeMnNi and CoCrNi is not negatively affected by decreasing the temperature, under plane strain conditions. A recent report made by Liu et al. [92] compared the cryogenic mechanical properties of CoCrNi to 316L and 316LN stainless steels. Tensile tests, impact toughness tests, and compact tension fracture toughness tests were performed at 293 and 77 K. The fracture toughness testing followed the same standard as by Gludovatz *et al.*. Their results showed a better impact toughness performance for CoCrNi compared to 316L(N) but a smaller K_{Ic} value at 77 K.

In this work, the fracture resistance of thin sheets was investigated under the scope of the essential work of fracture (EWF). One important question is to what extent EWF can be compared to J_{Ic}. Aside from the plane strain versus plane stress effects, w_e and J_{Ic} are not equivalent as J_{Ic} is related to cracking initiation, whereas the EWF method averages the work spent in the fracture process zone during the tearing process. If the propagation and initiation stages occur under the same mechanism and there is not much evolution in the degree of crack-tip necking from initiation to steady-state propagation, w_e can be compared to J_{Ic} [23]. This equivalence has been verified experimentally in polymers [66, 93] and in metallic alloys [22, 74]. However, even J_{Ic} is seldom reported at low temperature, even for conventional alloys. Table 2 presents some J_{Ic} values for several steels alongside the results reported by Gludovatz et al. [13, 14] for CoCrFeMnNi and CoCrNi. Contrary to how Cantor-based alloys are often portrayed in recent publications, both CoCrFeMnNi and CoCrNi are good at best. In order to connect the present work to (near-)plane-strain conditions, the work of damage Γ_0 can qualitatively be compared to fracture toughness values obtained in thick plates. We obtained values of Γ_0 ranging from 155 to 375 kJ.m^{-2} and ranging from 240 to 300 kJ.m^{-2} for CoCrFeMnNi at room temperature and 77 K, respectively, and values

Table 2: *Literature values for the fracture toughness at 77 Kfor the class of alloys studied in this study. J_{Ic} and K_{Ic} followed the ASTM E1820 [95] and E399 standards [96], respectively. Values with a star (∗) are estimated from K or J using $K = \sqrt{(E/1-\nu^2)J}$, with $\nu = 0.3$ and $E = 210$ [GPa].*

Alloy	J_{Ic} [kJ/m^2]	K_{Ic} [MPa.m$^{0.5}$]	Ref
AISI 304	241	230	[97]
	166*	196	[98]
AISI 310	210*	220	[99]
AISI 316	1150*	515	[99]
	100-700*	150-400	[100]
AISI 316L	975	449	[92]
	308	260	[97]
	623	370	[97]
AISI 316LN	500	200	[97]
	1193	522	[92]
AISI 321	220-700	220-400	[97]
Fe18Cr3Ni13Mn	76*	132	[99]
Fe21Cr12Ni5Mn	89*	144	[99]
Fe19Cr9Ni2Mn	323*	273	[99]
Fe21Cr6Ni9Mn	475*	331	[99]
Fe18Mn5Cr	340*	280	[101]
Fe9Ni	80*	135	[101]
Inconel 718	52	110	[102]
CoCrFeMnNi	255	219	[13]
CoCrNi	363	273	[14]

of ranging from 200 to 270 kJ.m^{-2} and ranging from 370 to 415 kJ.m^{-2} for CoCrNi at room temperature and 77 K, respectively. Gludovatz et al. reported 250 and 260 kJ.m^{-2} for CoCrFeMnNi and 210 and 270 kJ.m^{-2} for CoCrNi, at 293 and 77 K, respectively. In general, our Γ_0 values are moderately higher than the J_{Ic} of Gludovatz et al.. This can be explained by the low stress triaxiality associated to the stress state in the near-plane stress regime. In fact, $\Gamma_{0,plane\ stress}$ can be up to three times $J_{Ic,plane\ strain}$, see [20, 94]. Note that the results by Gludovatz et al. might not be associated to pure plane strain conditions and could potentially include some loss of constraint. It is also worth keeping in mind that while the same material is compared, the alloys differ in terms of initial void and inclusion contents and distributions, affecting also Γ_0.

The exploration of the cracking resistance of HEAs, especially at low temperature, is still very recent. MEAs and HEAs exhibit very good cracking resistance at low temperature based on compact tension [13, 14], hole-expansion [103], and Charpy impact [104–106] tests. However, a thorough review of the properties of MEAs/HEAs compared to state-of-the-art cryogenic alloys is still missing to consolidate the very positive fracture resistance performances claimed in recent literature, which are not fully confirmed in our study. The fracture toughness of metals failing by a ductile mechanism is primarily dependent on the initial inclusion content and on the inclusion spacing as well as on the yield strength and strain hardening capacity of the alloy [8, 9, 100]. There is no surprise that the J_{Ic} of a MEA/HEA very much varies with inclusion content and void nucleation resistance. In a recent study, we have shown that the failure of CoCrNi can be very well predicted using classical ductile fracture models [107] indicating no unusual failure mechanisms compared to more traditional alloys. The fact that the investigated Cantor-based alloys exhibit, as for stainless steels sheets, the classical failure mechanism by nucleation, growth, and coalescence of voids as well as significant necking at crack tip justified the use of the model to separate the two terms Γ_0 and Γ_n. The main outcome from the model is that stainless steels outperform Cantor-based alloys especially at low temperature due to their extreme values of strain hardening exponent. This result is expected to be true for thicknesses up to several millimetres with impact on many structural applications.

6 Conclusion

CoCrFeMnNi and CoCrNi are regarded in the literature as potential candidates for low temperature applications. The present work aimed at determining the tensile properties and the fracture resistance in thin sheet geometry of two high entropy alloys, CoCrFeMnNi and CoCrNi, and three reference conventional alloys, the 304L and 316L stainless steels and the Fe-Ni Invar alloy. Very good properties were confirmed for the Cantor-based alloys, but outperformed by the exceptional performances found for the stainless steels in the same conditions in terms of ductility, strength, and fracture resistance.

It is undeniable that MEAs and HEAs have opened new avenues in the development of novel alloys with different targeted performances. In the context of structural applications, particularly in cryogenic environment, where strength, ductility, and fracture toughness are important, Cantor alloys ultimately appear not better than conventional alloys. MEAs/HEAs will be more costly due to the chemical composition and complexity of processing. In any case, this study shows that the toughest alloys must be very clean (small f_0 and large X_0) with a large work hardening coefficient (n). This is particularly true for metal sheets due to the impact of the crack tip necking mechanism, while understanding that for very tough alloys, the near-plane-stress regime may extend up to thickness of 5 mm or more. A combination of the TRIP and TWIP effects are very effective to reach large strain hardening capacities, as generated in stainless steels. Although the history of stainless steels, including 304L and 316L, spans more than a century, there is still potential for further improvement beyond the already remarkable behaviour in order to better answer the challenges of tomorrow's low temperature applications.

Acknowledgements

The research was funded by the Walloon Region under the agreement No. 1610154-EntroTough in the context of the 2016 WallInnov call. Computational resources have been provided by the supercomputing facilities of the Université catholique de Louvain (CISM/UCLouvain) and the Consortium des Équipements de Calcul Intensif en Fédération Wallonie Bruxelles (CÉCI) funded by the Fond de la Recherche Scientifique de Belgique (F.R.S.-FNRS) under convention 2.5020.11 and by the Walloon Region. This work has been performed with the help of the Lacami technological platform of UCLouvain. The authors thank Valentin Marchal-Marchant for his help with the cryogenic tests. The authors gratefully acknowledge the support of the company APERAM for the supply of the 304L, 316L, and Invar sheets. The authors are also graceful to the Ecole des Mines of Saint-Etienne for the processing of three ingots with high purity.

References

[1] Giovanni Nicoletti, Natale Arcuri, Gerardo Nicoletti, and Roberto Bruno. A technical and environmental comparison between hydrogen and some fossil fuels. *Energy Conversion and Management*, 89:205–213, 2015.

[2] IP Jain. Hydrogen the fuel for 21st century. *International journal of hydrogen energy*, 34(17):7368–7378, 2009.

[3] Satish Kumar, Hyouk-Tae Kwon, Kwang-Ho Choi, Wonsub Lim, Jae Hyun Cho, Kyungjae Tak, and Il Moon. Lng: An eco-friendly cryogenic fuel for sustainable development. *Applied energy*, 88(12):4264–4273, 2011.

[4] UF Kocks and H Mecking. Physics and phenomenology of strain hardening: the fcc case. *Progress in materials science*, 48(3):171–273, 2003.

[5] T Ericsson. The temperature and concentration dependence of the stacking fault energy in the co-ni system. *Acta metallurgica*, 14(7):853–865, 1966.

[6] L_ Rémy, A Pineau, and B Thomas. Temperature dependence of stacking fault energy in close-packed metals and alloys. *Materials Science and Engineering*, 36(1):47–63, 1978.

[7] Bruno C De Cooman, Yuri Estrin, and Sung Kyu Kim. Twinning-induced plasticity (twip) steels. *Acta Materialia*, 142:283–362, 2018.

[8] André Pineau and Thomas Pardoen. Failure mechanisms of metals. *Comprehensive structural integrity encyclopedia*, 2:684–797, 2007.

[9] André Pineau, Amine A Benzerga, and Thomas Pardoen. Failure of metals i: Brittle and ductile fracture. *Acta Materialia*, 107:424–483, 2016.

[10] Viggo Tvergaard and John W Hutchinson. The relation between crack growth resistance and fracture process parameters in elastic-plastic solids. *Journal of the Mechanics and Physics of Solids*, 40(6):1377–1397, 1992.

[11] Thomas Pardoen and JW Hutchinson. Micromechanics-based model for trends in toughness of ductile metals. *Acta Materialia*, 51(1):133–148, 2003.

[12] Thomas Pardoen, Florence Scheyvaerts, Aude Simar, Cihan Tekoğlu, and Patrick R Onck. Multiscale modeling of ductile failure in metallic alloys. *Comptes Rendus Physique*, 11(3-4):326–345, 2010.

[13] Bernd Gludovatz, Anton Hohenwarter, Dhiraj Catoor, Edwin H Chang, Easo P George, and Robert O Ritchie. A fracture-resistant high-entropy alloy for cryogenic applications. *Science*, 345(6201):1153–1158, 2014.

[14] Bernd Gludovatz, Anton Hohenwarter, Keli VS Thurston, Hongbin Bei, Zhenggang Wu, Easo P George, and Robert O Ritchie. Exceptional damage-tolerance of a medium-entropy alloy crconi at cryogenic temperatures. *Nature communications*, 7:10602, 2016.

[15] Aditya Srinivasan Tirunilai, Jan Sas, Klaus-Peter Weiss, Hans Chen, Dorothée Vinga Szabó, Sabine Schlabach, Sebastian Haas, David Geissler, Jens Freudenberger, Martin Heilmaier, et al. Peculiarities of deformation of cocrfemnni at cryogenic temperatures. *Journal of Materials Research*, 33(19):3287–3300, 2018.

[16] Easo P George, Dierk Raabe, and Robert O Ritchie. High-entropy alloys. *Nature Reviews Materials*, 4(8):515–534, 2019.

[17] Easo P George, WA Curtin, and Cemal Cem Tasan. High entropy alloys: A focused review of mechanical properties and deformation mechanisms. *Acta Materialia*, 188:435–474, 2020.

[18] Dong Liu, Qin Yu, Saurabh Kabra, Ming Jiang, Paul Forna-Kreutzer, Ruopeng Zhang, Madelyn Payne, Flynn Walsh, Bernd Gludovatz, Mark Asta, et al. Exceptional fracture toughness of crconi-based medium-and high-entropy alloys close to liquid helium temperatures. *arXiv preprint arXiv:2204.01635*, 2022.

[19] David Broek. *The practical use of fracture mechanics*. Springer Science & Business Media, 2012.

[20] Thomas Pardoen, F Hachez, B Marchioni, PH Blyth, and AG Atkins. Mode i fracture of sheet metal. *Journal of the Mechanics and Physics of Solids*, 52(2):423–452, 2004.

[21] B Cotterell, Thomas Pardoen, and AG Atkins. Measuring toughness and the cohesive stress–displacement relationship by the essential work of fracture concept. *Engineering Fracture Mechanics*, 72(6):827–848, 2005.

[22] Thomas Pardoen, Yves Marchal, and Francis Delannay. Thickness dependence of cracking resistance in thin aluminium plates. *Journal of the Mechanics and Physics of Solids*, 47(10):2093–2123, 1999.

[23] Thomas Pardoen, Y Marchal, and Francis Delannay. Essential work of fracture compared to fracture mechanics—towards a thickness independent plane stress toughness. *Engineering Fracture Mechanics*, 69(5):617–631, 2002.

[24] D Frómeta, S Parareda, A Lara, S Molas, D Casellas, P Jonsén, and J Calvo. Identification of fracture toughness parameters to understand the fracture resistance of advanced high strength sheet steels. *Engineering Fracture Mechanics*, page 106949, 2020.

[25] RH Kropschot, RM McClintock, and DA Van Gundy. Mechanical properties of some engineering materials between 20 k and 300 k. In *Advances in Cryogenic Engineering*, pages 93–99. Springer, 1960.

[26] JG Kaufman, KO Bogardus, and ET Wanderer. Tensile properties and notch toughness of aluminum alloys at-452° f in liquid helium. In *Advances in Cryogenic Engineering*, pages 294–308. Springer, 1995.

[27] JL Christian and JF Watson. Mechanical properties of several 5000-series aluminum alloys at cryogenic temperatures. In *Advances in Cryogenic Engineering*, pages 490–499. Springer, 1962.

[28] JL Christian and JF Watson. Properties of 7000 series aluminum alloys at cryogenic temperatures. In *Advances in Cryogenic Engineering*, pages 604–621. Springer, 1961.

[29] JG Kaufman and ET Wanderer. Tensile properties and notch toughness of some 7xxx alloys at—452° f. In *Advances in Cryogenic Engineering*, pages 27–36. Springer, 1971.

[30] RP Mikesell and RP Reed. The impact testing of various alloys at low temperatures. In *Advances in Cryogenic Engineering*, pages 316–324. Springer, 1960.

[31] RP Mikesell and RP Reed. The tensile and impact strength of annealed and welded 5086 aluminum down to 20 k. In *Advances in Cryogenic Engineering*, pages 101–113. Springer, 1960.

[32] LP Rice, JE Campbell, and WF Simmons. Tensile behavior of parent-metal and welded 5000-series aluminum alloy plate at room and cryogenic temperatures. In *Advances in Cryogenic Engineering*, pages 478–489. Springer, 1962.

[33] A Everest. The behavior of high-magnesium-content aluminum alloys at room and liquid-nitrogen temperatures. In *Advances in Cryogenic Engineering*, pages 385–396. Springer, 1960.

[34] A Ya Ishchenko and NV Novikov. Mechanical properties of soviet and american al-mg alloy plates and welds for lng systems. In *Advances in Cryogenic Engineering*, pages 491–504. Springer, 1978.

[35] RA Kelsey and FG Nelson. Mechanical properties of us/ussr al-mg plate and welds for lng applications. In *Advances in Cryogenic Engineering*, pages 505–518. Springer, 1978.

[36] AW Pense, RD Stout, and BR Somers. Fracture toughness of cryogenic alloys. In *Advances in Cryogenic Engineering*, pages 548–559. Springer, 1978.

[37] Thomas S DeSisto and LC Carr. Low temperature mechanical properties of 300 series stainless steel and titanium. In *Advances in Cryogenic Engineering*, pages 577–586. Springer, 1961.

[38] W Weleff, HS McQueen, and WF Emmons. Cryogenic tensile properties of selected aerospace materials. In *Advances in Cryogenic Engineering*, pages 14–25. Springer, 1965.

[39] JL Christian and A Hurlich. Mechanical properties of titanium alloys at cryogenic temperatures. In *Advances in Cryogenic Engineering*, pages 318–333. Springer, 1995.

[40] KA Yushchenko. Low-temperature weldable steels and alloys. In *Advances in Cryogenic Engineering*, pages 120–128. Springer, 1978.

[41] James Watson and J Christian. Mechanical properties of high-strength 301 stainless steel sheet at 70,- 320, and- 423 f in the base metal and welded joint configuration. In *Symposium on Low-Temperature Properties of High-Strength Aircraft and Missile Materials*. ASTM International, 1961.

[42] CJ Guntner and Richard P Reed. Mechanical properties of four austenitic stainless steels at temperatures between 300° and 20° k. In *Advances in Cryogenic Engineering*, pages 565–576. Springer, 1961.

[43] S Jin, JW Morris, and VF Zackay. An iron-nickel-titanium alloy with outstanding toughness at cryogenic temperature. In *Advances in Cryogenic Engineering*, pages 379–384. Springer, 1995.

[44] RL Tobler, RP Reed, and DS Burkhalter. Temperature dependence of yielding in austenitic stainless steels. In *Advances in cryogenic engineering materials*, pages 107–119. Springer, 1980.

[45] JM Wells, WA Logsdon, and R Kossowsky. Evaluation of weldments in austenitic stainless steels for cryogenic applications. In *Advances in Cryogenic Engineering*, pages 150–160. Springer, 1978.

[46] CL Goodzeit. Evaluation of stainless steel casting alloys for cryogenic service in the 80-inch liquid-hydrogen bubble chamber. In *Advances in Cryogenic Engineering*, pages 26–36. Springer, 1965.

[47] JP Bruner and DA Sarno. An evaluation of three steels for cryogenic service. In *Advances in Cryogenic Engineering*, pages 529–539. Springer, 1978.

[48] RL Tobler, HI McHenry, and RP Reed. Fracture mechanics parameters for an iron-13% chromium-19% manganese stainless steel and its welds at cryogenic temperatures. In *Advances in Cryogenic Engineering*, pages 560–572. Springer, 1978.

[49] FN Mazandarany, DM Parker, RF Koenig, and DT Read. A nitrogen-strengthened austenitic stainless steel for cryogenic magnet structures. In *Advances in Cryogenic Engineering Materials*, pages 158–170. Springer, 1980.

[50] FS Death and HM Long. The low-temperature mechanical properties of some selected austenitic manganese steels. In *Advances in Cryogenic Engineering*, pages 421–429. Springer, 1960.

[51] JW Morris, SK Hwang, KA Yushchenko, VI Belotzerkovetz, and OG Kvasnevskii. Fe-mn alloys for cryogenic use: a brief survey of current research. *Advances in Cryogenic Engineering*, pages 91–102, 1978.

[52] S Tone, M Shimada, T Horiuchi, Y Kasamatsu, H Nakajima, and S Shimamoto. The development of a nitrogen-strengthened high-manganese austenitic stainless steel for a large superconducting magnet. In *Advances in Cryogenic Engineering Materials*, pages 145–152. Springer, 1984.

[53] JL Christian. Mechanical properties of several nickel-base alloys at room and cryogenic temperatures. *Advance Cryogenic Eng*, 12:520–531, 1966.

[54] WA Logsdon, R Kossowsky, and JM Wells. The influence of processing and heat treatment on the cryogenic fracture mechanics properties of inconel 718. In *Advances in Cryogenic Engineering*, pages 197–209. Springer, 1978.

[55] WA Logsdon, JM Wells, and R Kossowsky. Cryogenic fracture toughness and fatigue crack-growth rate properties of inconel 706 base material and gas tungsten-arc weldments. In *Advances in Cryogenic Engineering Materials*, pages 137–150. Springer, 1980.

[56] HL Eiselstein. An age-hardenable, low-expansion alloy for cryogenic service. In *Advances in Cryogenic Engineering*, pages 508–519. Springer, 1967.

[57] HI McHenry and RE Schramm. Note on the fracture properties of fe-49ni at cryogenic temperatures. In *Advances in Cryogenic Engineering*, pages 161–165. Springer, 1978.

[58] J Savas. The fe-10ni-1mo-0.20 c steel as a potential alloy for cryogenic applications. In *Advances in Cryogenic Engineering Materials*, pages 126–136. Springer, 1980.

[59] Laurine Choisez, Ahmed Elmahdy, Patricia Verleysen, and PJ Jacques. Fracture mechanisms in flat and cylindrical tensile specimens of trip-twip β-metastable ti-12mo alloy. *Acta Materialia*, 220:117294, 2021.

[60] ZL Zhang, M Hauge, J Ødegård, and C Thaulow. Determining material true stress–strain curve from tensile specimens with rectangular cross-section. *International Journal of Solids and Structures*, 36(23):3497–3516, 1999.

[61] JM Choung and SR Cho. Study on true stress correction from tensile tests. *Journal of Mechanical Science and Technology*, 22(6):1039–1051, 2008.

[62] B Cotterell and JK Reddel. The essential work of plane stress ductile fracture. *International journal of fracture*, 13(3):267–277, 1977.

[63] KB Broberg. The importance of stable crack extension in linear and nonlinear fracture mechanics. *Paper from" Prospects of Fracture Mechanics". Noordhoff International Publishing, Leyden, Netherlands. 1974, 125-137.*, 1974.

[64] KB Broberg. On stable crack growth. *Journal of the Mechanics and Physics of Solids*, 23(3):215–237, 1975.

[65] Yves Marchal, Jean-François Walhin, and Francis Delannay. Statistical procedure for improving the precision of the measurement of the essential work of fracture of thin sheets. *International Journal of Fracture*, 87(2):189–199, 1997.

[66] Marta Rink, Luca Andena, and Claudia Marano. The essential work of fracture in relation to j-integral. *Engineering Fracture Mechanics*, 127:46–55, 2014.

[67] Antoine Hilhorst, Thomas Pardoen, and PJ Jacques. Optimization of the essential work of fracture method for characterization of the fracture resistance of metallic sheets. *Engineering Fracture Mechanics*, 268:108442, 2022.

[68] Thomas Pardoen and JW Hutchinson. An extended model for void growth and coalescence. *Journal of the Mechanics and Physics of Solids*, 48(12):2467–2512, 2000.

[69] Kim Lau Nielsen and John W Hutchinson. Cohesive traction–separation laws for tearing of ductile metal plates. *International Journal of Impact Engineering*, 48:15–23, 2012.

[70] EP George, WA Curtin, and CC Tasan. High entropy alloys: A focused review of mechanical properties and deformation mechanisms. *Acta Materialia*, 2019.

[71] Laurine Choisez, Lipeng Ding, Matthieu Marteleur, Hosni Idrissi, Thomas Pardoen, and PJ Jacques. High temperature rise dominated cracking mechanisms in ultra-ductile and tough titanium alloy. *Nature communications*, 11(1):1–8, 2020.

[72] Stefan Golling, David Frómeta, Daniel Casellas, and Pär Jonsén. Investigation on the influence of loading-rate on fracture toughness of ahss grades. *Materials Science and Engineering: A*, 726:332–341, 2018.

[73] ZC Luo and MX Huang. Revealing the fracture mechanism of twinning-induced plasticity steels. *steel research international*, 89(9):1700433, 2018.

[74] G Lacroix, Thomas Pardoen, and Pascal J Jacques. The fracture toughness of trip-assisted multi-phase steels. *Acta Materialia*, 56(15):3900–3913, 2008.

[75] SK Chandra, R Sarkar, AD Bhowmick, PS De, PC Chakraborti, and SK Ray. Fracture toughness evaluation of interstitial free steel sheet using essential work of fracture (ewf) method. *Engineering Fracture Mechanics*, 204:29–45, 2018.

[76] B Chehab, Y Brechet, J-C Glez, PJ Jacques, J-D Mithieux, M Veron, and Thomas Pardoen. Characterization of the high temperature tearing resistance using the essential work of fracture—application to dual phase ferritic stainless steels. *Scripta Materialia*, 55(11):999–1002, 2006.

[77] Daniel Casellas, Antoni Lara, David Frómeta, David Gutiérrez, Sílvia Molas, Lluís Pérez, Johannes Rehrl, and Clemens Suppan. Fracture toughness to understand stretch-flangeability and edge cracking resistance in ahss. *Metallurgical and Materials Transactions A*, 48(1):86–94, 2017.

[78] D Frómeta, M Tedesco, J Calvo, A Lara, S Molas, and Daniel Casellas. Assessing edge cracking resistance in ahss automotive parts by the essential work of fracture methodology. In *Journal of Physics: Conference Series*, volume 896, page 012102. IOP Publishing, 2017.

[79] Subhadra Sahoo, N Padmapriya, Partha Sarathi De, PC Chakraborti, and SK Ray. Ductile tearing resistance indexing of automotive grade dp 590 steel sheets: Ewf testing using dent specimens. *Journal of Materials Engineering and Performance*, 27(4), 2018.

[80] Stefan Golling, David Frómeta, Daniel Casellas, and Pär Jonsén. Influence of microstructure on the fracture toughness of hot stamped boron steel. *Materials Science and Engineering: A*, 743:529–539, 2019.

[81] YW Mai and KM Pilko. The essential work of plane stress ductile fracture of a strain-aged steel. *Journal of materials science*, 14(2):386–394, 1979.

[82] YW Mai and B Cotterell. Effect of specimen geometry on the essential work of plane stress ductile fracture. *Engineering fracture mechanics*, 21(1):123–128, 1985.

[83] MP Wnuk and DT Read. Essential work of fracture (we) versus energy dissipation rate (j c) in plane stress ductile fracture. *International journal of fracture*, 31(3):161–171, 1986.

[84] Karim Ismail, Astrid Perlade, Pascal J Jacques, and Thomas Pardoen. Outstanding cracking resistance of fibrous dual phase steels. *Acta Materialia*, 207:116700, 2021.

[85] RT Hill. On discontinuous plastic states, with special reference to localized necking in thin sheets. *Journal of the Mechanics and Physics of Solids*, 1(1):19–30, 1952.

[86] AR Shahani, M Rastegar, M Botshekanan Dehkordi, and H Moayeri Kashani. Experimental and numerical investigation of thickness effect on ductile fracture toughness of steel alloy sheets. *Engineering Fracture Mechanics*, 77(4):646–659, 2010.

[87] G Laplanche, A Kostka, C Reinhart, J Hunfeld, G Eggeler, and EP George. Reasons for the superior mechanical properties of medium-entropy crconi compared to high-entropy crmnfeconi. *Acta Materialia*, 128:292–303, 2017.

[88] Lipeng Ding, Antoine Hilhorst, Hosni Idrissi, and PJ Jacques. Potential trip/twip coupled effects in equiatomic crconi medium-entropy alloy. *Acta Materialia*, page 118049, 2022.

[89] Jiashi Miao, CE Slone, TM Smith, C Niu, Hongbin Bei, M Ghazisaeidi, GM Pharr, and Michael J Mills. The evolution of the deformation substructure in a ni-co-cr equiatomic solid solution alloy. *Acta Materialia*, 132:35–48, 2017.

[90] Richard P Reed. Low-temperature tensile properties of fe-ni alloys. *Advances in Cryogenic Engineering Materials*, pages 25–32, 1998.

[91] HP Reed. Martensitic transformations in fe-cr-ni stainless steels. *Austenitic Steels at Low Temperatures*, pages 41–67, 1983.

[92] Xiaoru Liu, Hao Feng, Jing Wang, Xuefei Chen, Ping Jiang, Fuping Yuan, Huabing Li, En Ma, and Xiaolei Wu. Mechanical property comparisons between crconi medium-entropy alloy and 316 stainless steels. *Journal of Materials Science & Technology*, 2021.

[93] Daniel Vavrik and Ivan Jandejsek. Experimental evaluation of contour j integral and energy dissipated in the fracture process zone. *Engineering Fracture Mechanics*, 129:14–25, 2014.

[94] Thomas Siegmund and Wolfgang Brocks. Prediction of the work of separation and implications to modeling. *International Journal of Fracture*, 99:97–116, 1999.

[95] ASTM E1820-01. Standard test method for measurement of fracture toughness. Technical report, ASTM, 2001.

[96] ASTM E399-12. Standard test method for linear-elastic plane-strain fracture toughness kic of metallic materials. Technical report, ASTM, 2012.

[97] H Krauth and A Nyilas. Toughness and fatigue properties of austenitic steels at cryogenic temperature and their application in complex structures. In *Austenitic Steels at Low Temperatures*, pages 159–169. Springer, 1983.

[98] Krishnaswamy Sampath, Thomas Drube, and Mahendra Rana. A reaffirmation of fracture toughness requirements for asme section viii vessels for service temperatures colder than 77 k. *Journal of Pressure Vessel Technology*, 139(4), 2017.

[99] HI McHenry. The properties of austenitic stainless steel at cryogenic temperatures. In *Austenitic Steels at Low Temperatures*, pages 1–27. Springer, 1983.

[100] RL Tobler, A Nishimura, and J Yamamoto. Design-relevant mechanical properties of 316-type steels for superconducting magnets. *Cryogenics*, 37(9):533–550, 1997.

[101] R Miura, K Ohnishi, H Nakajima, Y Takahashi, and K Yoshida. Mechanical properties of 18mn-5cr austenitic steel at cryogenic temperatures. In *Austenitic Steels at Low Temperatures*, pages 287–293. Springer, 1983.

[102] RL Tobler. Low temperature effects on the fracture behaviour of a nickel base superalloy. *Cryogenics*, 16(11):669–674, 1976.

[103] Yeon Taek Choi, Jae Wung Bae, Jeong Min Park, Hak Hyeon Lee, Hyeonseok Kwon, Sujung Son, Dong-Hyun Ahn, and Hyoung Seop Kim. Stretch-flangeability of cocrfemnni high-entropy alloy. *Materials Science and Engineering: A*, 814:141241, 2021.

[104] DongYue Li and Yong Zhang. The ultrahigh charpy impact toughness of forged alxcocrfeni high entropy alloys at room and cryogenic temperatures. *Intermetallics*, 70:24–28, 2016.

[105] SQ Xia, MC Gao, and Y Zhang. Abnormal temperature dependence of impact toughness in alxcocrfeni system high entropy alloys. *Materials Chemistry and Physics*, 210:213–221, 2018.

[106] Xiaolei Wu, Muxin Yang, Ping Jiang, Chang Wang, Lingling Zhou, Fuping Yuan, and Evan Ma. Deformation nanotwins suppress shear banding during impact test of crconi medium-entropy alloy. *Scripta Materialia*, 178:452–456, 2020.

[107] Antoine Hilhorst, Julien Leclerc, Thomas Pardoen, Pascal J Jacques, Ludovic Noels, and Van-Dung Nguyen. Ductile fracture of high entropy alloys: From the design of an experimental campaign to the development of a micromechanics-based modeling framework. *Engineering Fracture Mechanics*, 275:108844, 2022.